Electronic Supplementary Information

Confinement twists achiral liquid crystals and causes chiral liquid crystals to twist in the opposite direction: Cases in and around sessile droplets

Jungmyung Kim and Joonwoo Jeong

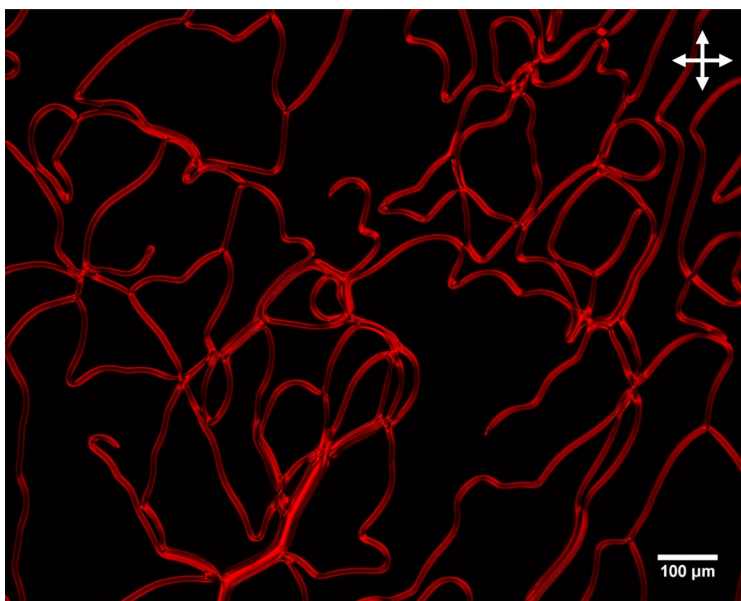## Fingerprint texture at a high concentration of the chiral dopant

Figure S1: The polarized optical microscopy (POM) image of 30.0% (wt/wt) sunset yellow (SSY) with 0.5% (wt/wt) brucine sulfate hydrate (BSH) in our sandwich cell at room temperature with crossed polarizers. White double arrows represent the crossed polarizers. The scale bar is 100 μm.

The fingerprint texture appears at high dopant concentrations. Nematic directors at dark regions are homeotropically aligned. In contrast, despite the homeotropic anchoring at the top and bottom substrates, the directors in bright stripes — the onset of the chiral nematic's fingerprint texture — are twisted because of the chiral dopants. Thus, we conduct the sessile droplet experiments only at low dopant concentrations where a uniform dark background with no stripes is guaranteed.

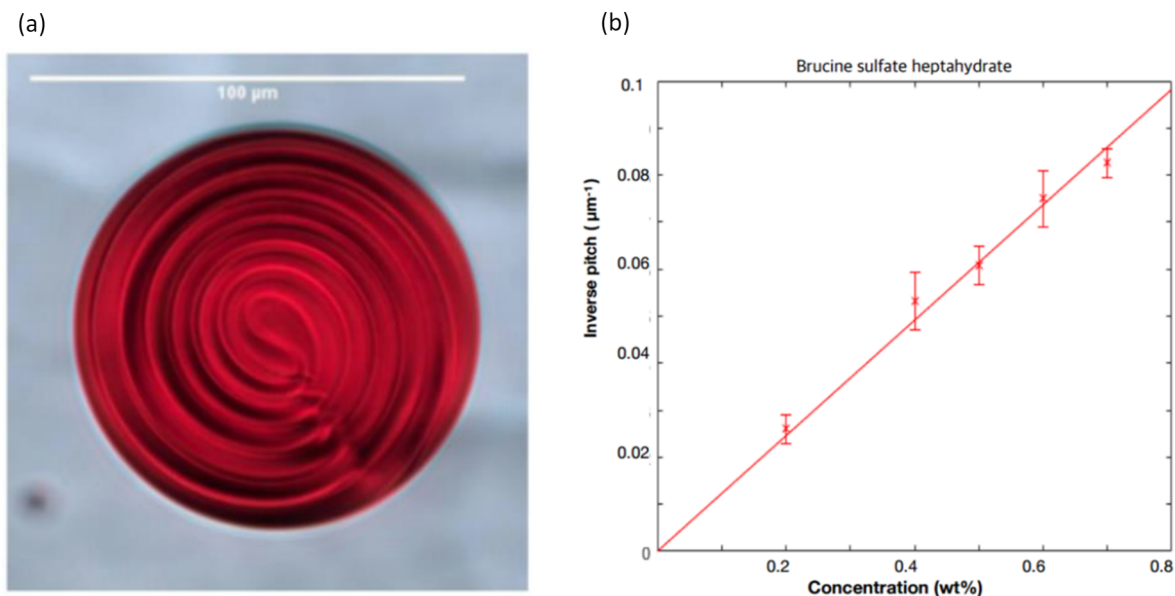# Measurement of helical twisting power of brucine sulfate hydrate

(a)

(b)

Figure S2: **(a)** The bright field microscope image of a droplet of 30.0% (wt/wt) SSY doped with BSH. **(b)** The measured inverse pitches as a function of the chiral dopant concentration.

The helical twisting power of BSH in 30.0% (wt/wt) SSY is measured using fingerprint textures in spherical droplets. As shown in Fig. S2(a), a BSH-doped SSY droplet dispersed in silicon oil exhibits the fingerprint texture with a measurable helical pitch. Note that the repeating distance is the half pitch along which the nematic directors rotate by 180 degrees. At various chiral dopant concentrations, the helical pitches are measured, and its inverse pitches are plotted as shown in Fig. S2(b). The slope of the linear fit shown as a solid line gives the helical twisting power, 0.123 ± 0.007 μm^{-1}. This data is adopted from the Master thesis (2019) of Leekyo Jung from Ulsan National Institute of Science and Technology
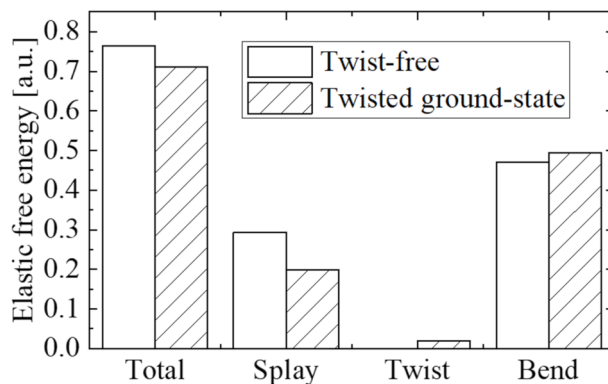
Rationalization of the director field models

Figure S3: Comparison of elastic free energy between the twist-free planar quadrupole and the energy-minimizing twisted director configuration. We numerically found the twisted ground state from our ansatz for the I-in-N system, which is introduced in the main text with Eqs. (1-3). The twisted configuration lowers its total elastic free energy by decreasing splay energy more than the twist and bend penalty.

Chiral symmetry breaking in confined LCLC has been reported in the literature. Splay cancellation by the twist deformation is one of the well-known underlying mechanisms for this phenomenon because lyotropic LCs usually have a smaller twist modulus than other moduli. Particularly, when confined, the region near the defects plays a key role because the splay and/or bend deformation is concentrated near them. In other words, twist deformation can also be concentrated near the defect to cancel out the expensive energetic cost of the splay or bend deformation. This inspires us to adopt decaying functions to impose twist deformation to twist-free configuration, *e.g.*, the planar quadrupole configuration. As in Eq. 4 of our main text, we design our twist ansatz so that the degree of the twist deformation decreases as the position gets away from the defect while satisfying the boundary conditions. Specifically, we compare the exponential and power-law decaying functions to find that the power-law function results in a lower total energy (data not shown). Note that this is an improved model compared to the simple linear twist model in Ref. 10. As a result, we show in Fig. S3 that the splay cancellation indeed underlies the chiral symmetry breaking.

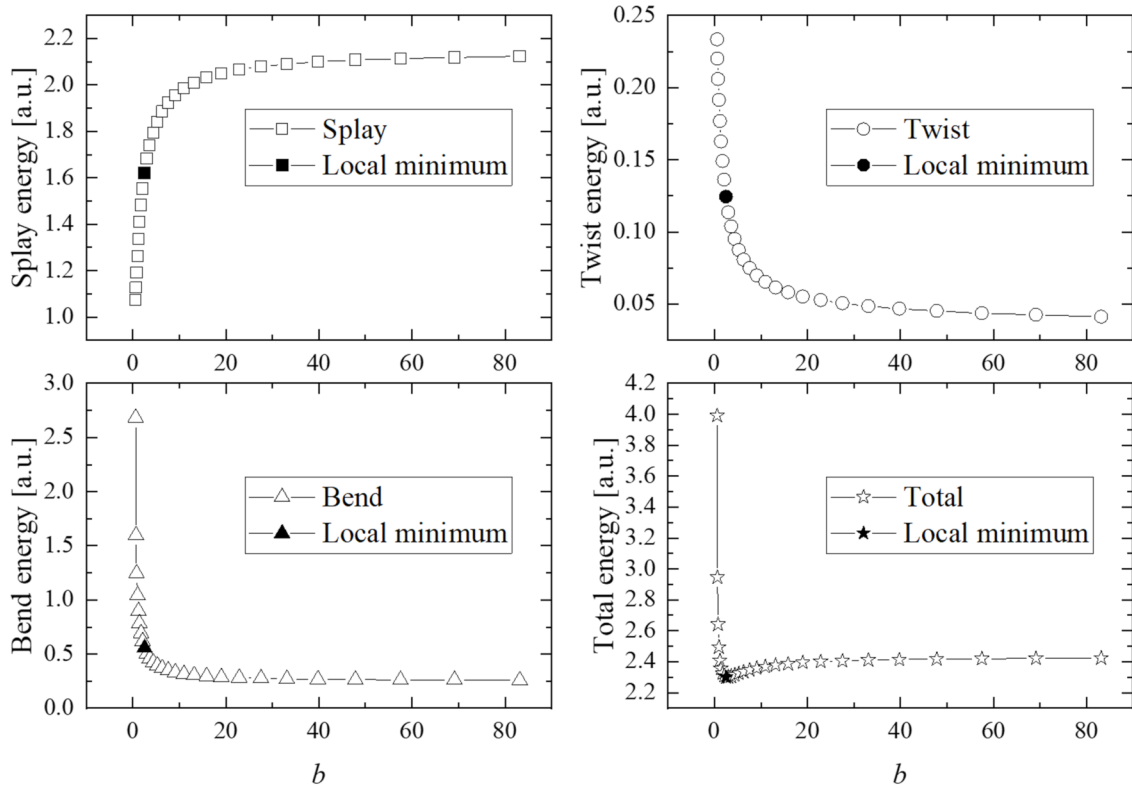# Energy landscape in the vicinity of the local minimum in the N-in-I system

Figure S4: The energy landscape in the vicinity of the local minimum configuration having the disfavored handedness in the N-in-I system. To rationalize the existence of the local minimum, we investigate how the energy — splay, twist, bend, and total, respectively — changes according to the model parameter b near the local minimum ($a = 90$, $b = 2.51$, and $c = 0.23$) of the system having 0.1% (wt/wt) of BSH and $K_1 = K_3 = 10 \, K_2$. This calculation demonstrates that the competition among splay, twist, and bend is responsible for the local minimum, even in the region of the disfavored handedness. Namely, the splay decreases as b gets smaller while twist and bend change in the opposite way, resulting in the local minimum.

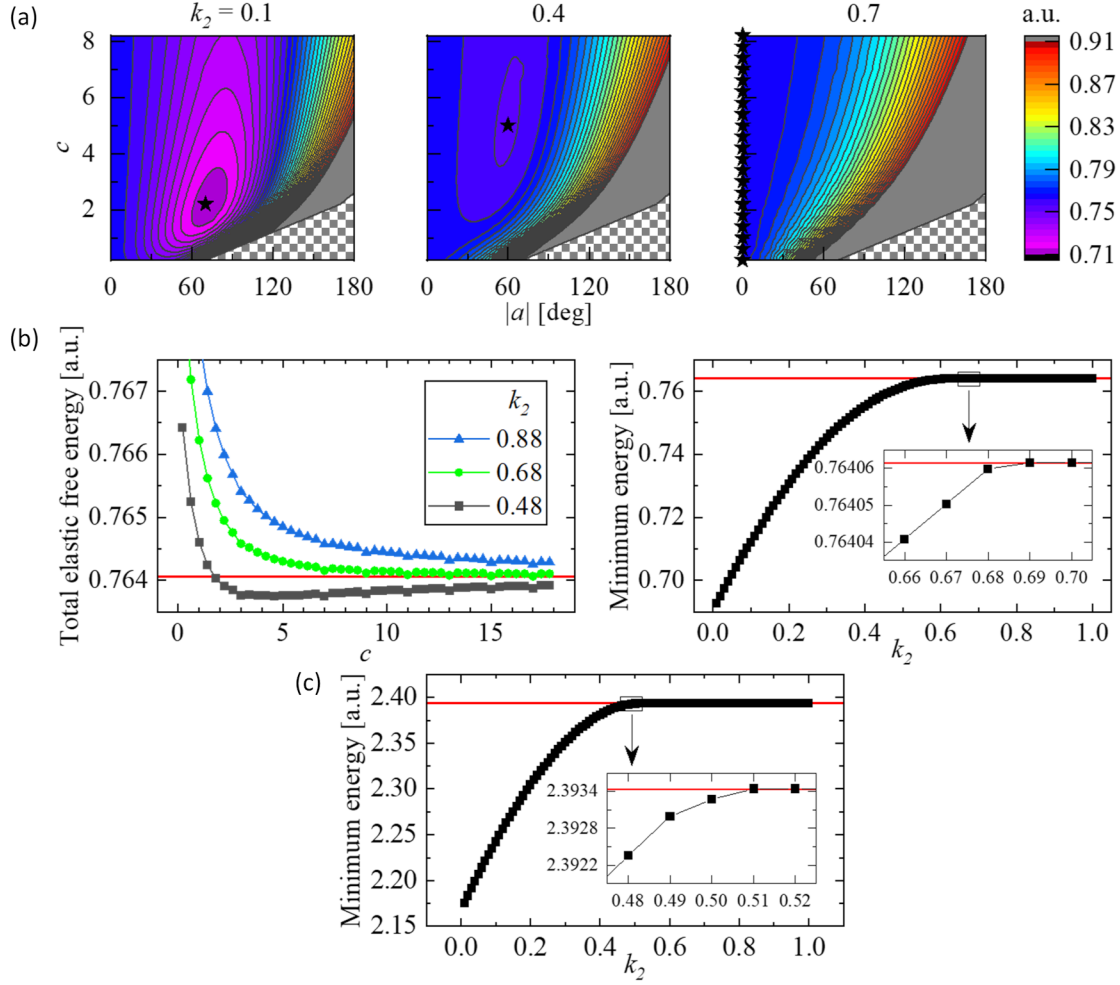# Determination of critical k_2 for the chiral symmetry breaking

Figure S5: critical k_2 for the chiral symmetry breaking **(a)** The elastic free energy landscapes in the I-in-N system according to $k_2 = K_2/K_3$: 0.1, 0.4 and 0.7, respectively. The filled star symbols indicate the minima. **(b)** The determination of the critical k_2 for the chiral symmetry breaking in the I-in-N system using two different approaches. The left graph varies the ansatz parameter c at a given $a = 10$ and k_2 and compares the total elastic free energy of the twisted configuration with the energy of the twist-free configuration. The right graph plots the smallest total elastic free energy, *i.e.*, the global minimum value in the energy landscape according to k_2; the red line is the of the twist-free configuration. **(c)** The determination of the critical k_2 for the chiral symmetry breaking in the N-in-I system.

In Fig. S5(a), we calculate numerically the elastic free energy landscapes in the a-c parameter space of the ansatz depending on different $k_2 = K_2/K_3$ values: 0.1, 0.4, and 0.7. They show that the twisted ground state with the finite a exists only when k_2 is small enough; Filled star symbols indicate the energy minima. For instance, with $k_2 = 0.7$, the twist-free director configuration with $a = 0$ is the ground state. This indicates that the chiral-symmetry-breaking transition point exists between $k_2 = 0.4$ and 0.7. Note that the checkerboard-patterned areas on the right-bottom regions are excluded since director configurations in those regimes considerably violate the boundary conditions.

To narrow down the chiral-symmetry-breaking transition point, we investigate the energy landscape in detail. First, we focus on the shape change from a double-well landscape — symmetric about $a = 0$ with two global minima — to a single-well shape having one global minimum, which corresponds to the twist-free configuration. To capture this transition while varying k_2, we calculate

the energy profile along c at the regime next to the symmetric axis. The left graph of Fig. S5(b) plots these according to k_2. We find that only when k_2 becomes smaller than 0.68, there exists at least one (a, c) of which the energy is smaller than the twist-free configuration, which leads to the double-well landscape about $a = 0$.

We find the same critical k_2 value from another method. We investigate the global minimum energy value over the energy landscape as a function of k_2 and find that the minimum value can be smaller than the energy of the twist-free configuration when $k_2 \leq 0.68$, as shown in the right graph of Fig. S5(b). As shown in Fig. S5(c), we apply the same approach to the N-in-I system to find $k_{\mathrm{crit}} = 0.50$.

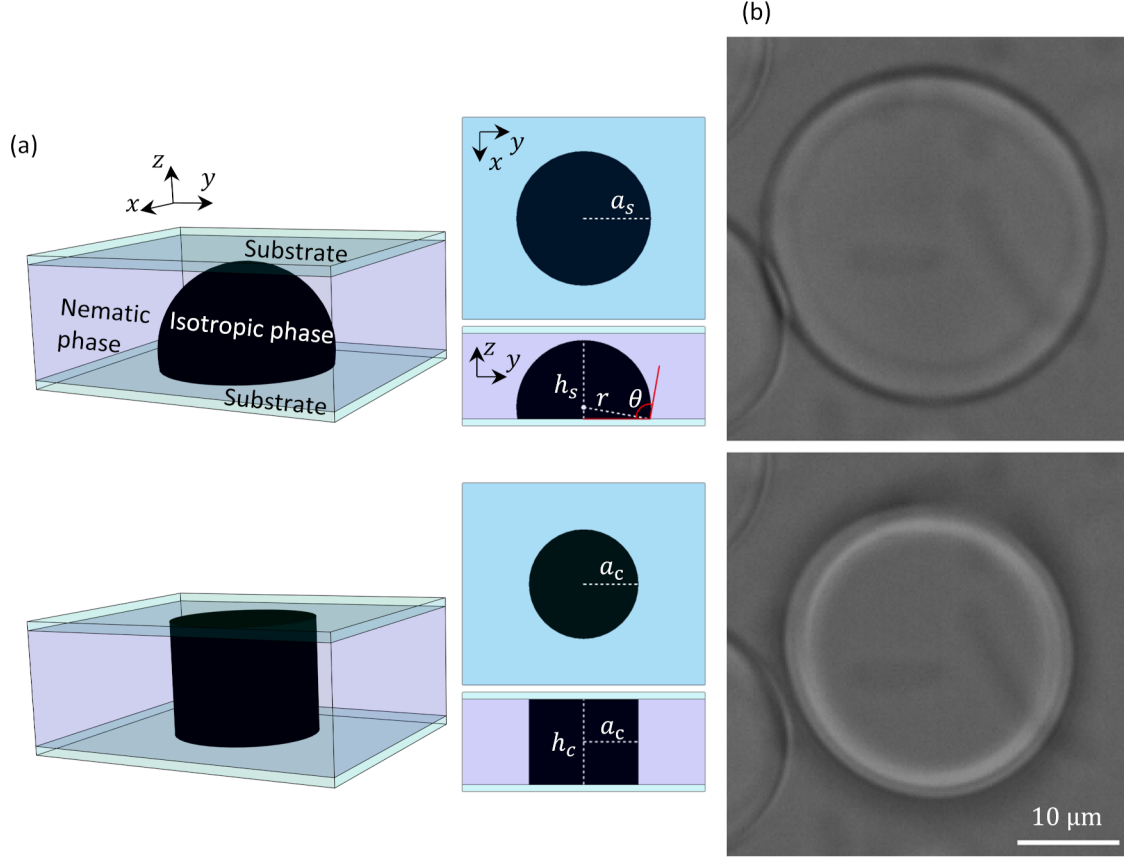# Estimation of contact angle and shape of sessile droplets

Figure S6: The schematic diagram and the representative experimental results for the estimation of the sessile droplets' contact angle on the parylene-coated glass. **(a)** Schematic diagrams of (Top) a sessile droplet sitting at the bottom substrate and (Bottom)a cylindrical droplet connecting the top and bottom substrates. a_s and h_s are the base radius and height of the sessile droplet, respectively. r is the radius of the spherical cap, and θ is the contact angle. a_c and h_c are the base radius and height of the cylindrical droplet, respectively. **(b)** Comparison of bright-field images (Top) before and (Bottom) after the transition from the spherical cap to the cylinder. The spherical cap-shaped droplet is surrounded by a dark line, while the cylinder shows a bright boundary.

Because the experimental geometry does not allow side-view imaging nor confocal microscopy for the direct imaging of the droplet shape, we estimate indirectly the contact angle utilizing the transition from the spherical-cap droplet to the cylindrical droplet. As shown in Fig. S6(a), the contact angle θ is related to the height and radius of the sessile droplet having the spherical-cap shape: $\theta = 90° + \sin^{-1}\frac{h_\mathrm{s}-r}{r}$, where $h_\mathrm{s} > r$ with $\theta \geq 90$ degrees. The volume V_s of the spherical cap can be written using a_s and h_s: $\frac{1}{6}h_\mathrm{s}(3(\pi a_\mathrm{s}^2) + \pi h_\mathrm{s}^2) = V_\mathrm{s}$. We measure experimentally the area $\pi a_\mathrm{s}^2 = A_\mathrm{s}$. After the transition of the spherical cap to the cylinder spanning the cell gap, we measure experimentally another area $\pi a_\mathrm{c}^2 = A_\mathrm{c}$. Assuming the cylinder is straight based on the BF image after the transition, we write the cylinder volume $V_\mathrm{c} = (\pi a_\mathrm{c}^2)h_\mathrm{c}$. The transition from the spherical cap to the cylinder implies that $h_\mathrm{s} \approx h_\mathrm{c}$ is approximately the height h of the sandwich cell, and the volume is conserved, *i.e.*, $V_\mathrm{s} = V_\mathrm{c}$. Thus, we determine the $h = h_\mathrm{s} = h_\mathrm{c}$ and $r = \sqrt{(h - r)^2 + a_\mathrm{s}^2}$, to find θ. We find the contact angle is slightly greater than 90°: 97.1 and 98.4° from two independent measurements. The corresponding height h are 18.7 and 21.6 μm, which are not much different from the thickness of the spacer, 25 μm.